ELSEVIER

Journal of Marine Systems 35 (2002) 207–227

JOURNAL OF MARINE SYSTEMS

www.elsevier.com/locate/jmarsys

On the dense water spreading off the Ross Sea shelf (Southern Ocean)

G. Budillon [a], S. Gremes Cordero [b], E. Salusti [c,*]

[a] *Istituto di Metereologia e Oceanografia - Università di Napoli "Parthenope", Via Acton, 38, 80133 Napoles, Italy*
[b] *Dipartimento di Fisica, Università di Roma "La Sapienza", Piazzale Aldo Moro 2, 00185 Rome, Italy*
[c] *Istituto Nazionale di Fisica Nucleare - Dipartimento di Fisica, Università di Roma "La Sapienza", Piazzale Aldo Moro 2, 00185 Rome, Italy*

Received 29 March 1999; accepted 27 January 2002

Abstract

In this study, current meter and hydrological data obtained during the *X* Italian Expedition in the Ross Sea (CLIMA Project) are analyzed. Our data show a nice agreement with previous data referring to the water masses present in this area and their dynamics. Here, they are used to further analyze the mixing and deepening processes of Deep Ice Shelf Water (DISW) over the northern shelf break of the Ross Sea. In more detail, our work is focused on the elementary mechanisms that are the most efficient in removing dense water from the shelf: either classical mixing effects or density currents that interact with some topographic irregularity in order to drop to deeper levels, or also the variability of the Antarctic Circumpolar Current (ACC) which, in its meandering, can push the dense water off the shelf, thus interrupting its geostrophic flow. We also discuss in detail the (partial) evidence of dramatic interactions of the dense water with bottom particulate, of geological or biological origin, thus generating impulsive or quasi-steady density-turbidity currents. This complex interaction allows one to consider bottom particular and dense water as a unique self-interacting system. In synthesis, this is a first tentative analysis of the effect of bottom particulate on the dense water dynamics in the Ross Sea.

Keywords: Dense water dynamics; Bottom particulate; Ross Sea

1. Introduction

The study of the different processes involved in the dynamics of the Southern Ocean has been intensified in the last few years, due to their importance in influencing the world ocean circulation and the global climate. Being the only ocean in which marine currents run completely around the globe, as atmospheric currents do, it can be seen as a gateway between oceanographic and meteorological circulation models.

The Southern Ocean is bounded by the Antarctic continent to the south; the Subtropical Front is traditionally considered as its northern limit. One important dynamic feature of this ocean is the Antarctic Circumpolar Current (ACC, in the following) which moves west to east around Antarctica, interacting with different water masses. It carries the Circumpolar Deep Water (CDW, in the following), a voluminous water mass that extends down to a depth of $\sim$ 4000 m.

South of the ACC are vast areas of sluggish flow, where the dynamic height anomaly of the sea surface, relative to 2500 m, identifies the Ross Gyre extending between 160°E and 140°W (Fig. 1). Note how also part of the CDW flows into the Ross Gyre and, on

* Corresponding author. Tel.: +39-06-49914291; fax: +39-06-4957697.
E-mail address: ettore.salusti@roma1.infn.it (E. Salusti).

0924-7963/02/$ - see front matter
PII: S0924-7963(02)00082-9

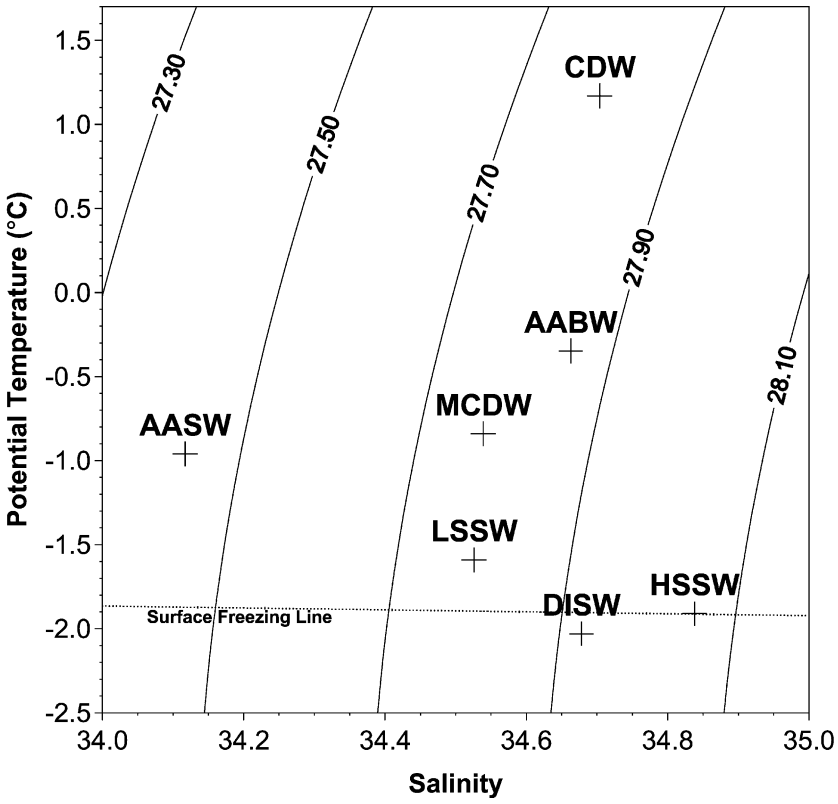

Fig. 1. Synthetic $\theta-S$ diagram for water types in the Ross Sea (see text for acronyms).

reaching the Antarctic continental shelf break, is forced to move upward and so mixes with the shelf waters. This mixing forms a distinct water mass, the Modified Circumpolar Deep Water (MCDW), characterized in this region by a subsurface potential temperature maximum and dissolved oxygen minimum. It is interesting how MCDW interacts actively with the ice and the cold atmosphere (Budillon et al., 2000; Budillon and Spezie, 2000) to form shelf waters in the Ross Sea, as the Deep Ice Shelf Water (DISW), characterized by a temperature lower than the surface freezing point (Jacobs et al., 1985; Trumbore et al., 1991; Locarnini, 1994; Hofman and Klink, 1998; Fig. 1).

These dense shelf waters and their thermodynamics are analyzed here, with particular reference to their northward motion. Indeed, at the northern shelf break of the Ross Sea, they apparently disappear, sinking towards the deepest layers. In general, deep or bottom water in Polar Oceans is traditionally schematized as being formed by two main processes, namely through convective overturning and mixing when the water column becomes vertically unstable, and through deep thermohaline overturning, which depends on the horizontal density gradient (Harvey, 1996). A third process is generally taken into less consideration, namely the formation of dense water masses over the shelves, followed by their downslope flow along sharp submarine canyons (Killworth, 1983). In this study, we therefore analyze some recent hydrological and current meter data collected by the Italian CLIMA Project on the Ross Sea in 1995. Our interest is focused precisely on the mechanisms driving the sinking of these dense waters from the Ross Sea shelf. Obviously, this does not depend on a single process but on a combination of several. This study consequently gives a critical description of the mechanisms contributing to this evolution of dense shelf waters and focus the attention on the (partial) evidence of strong current–bottom particulate interaction. Thus, in Section 2, the Ross Sea hydrology is analyzed, and in

Section 3, our data are briefly summarized. More details on CTD casts and current meter data are given in Section 4, and in Section 5, a general discussion is made of recent models. These are applied to our data on the Ross Sea dynamics, and discussed in the concluding sections.

2. The Ross Sea: geographical and hydrological characteristics

The Ross Sea is located in the Pacific sector of the Southern Ocean, between Cape Colbeck at 158°W and Cape Adare at 170°E (Fig. 2). On the southern side it is bounded by the Ross Ice Shelf, at around 78.5°S. This broad ice cover, which extends over nearly half the continental shelf, is about 250 m thick on its northernmost side (Jacobs, 1989). This Ross Ice Shelf therefore only limits the uppermost waters, while deep waters can circulate freely under the floating ice shelf.

The central western sector of the Ross Sea is characterized by alternating reliefs and depressions, some of which are deeper than the platform edge. Indeed, the bottom topography in this zone is rather irregular, with the ~ 500 m deep shelf isolated from the shore by a canyon oriented northeastward and deeper than 1000 m, the Drygalski Basin.

Recently, Locarnini (1994) found that the subsurface circulation of the Ross sea is formed by two different cyclonic gyres at its eastern and western limits, connected by a U-shaped cyclonic feature in the vicinity of the Ross Ice Shelf front. In addition, more recent current meter measurements revealed an important mesoscale activity, with a mild seasonal variability (Jaeger et al., 1996; Picco et al., 1999).

Of particular interest on climatological or oceanographic grounds are the dense shelf waters in the Ross Sea: these are formed during the Austral winter when the upper layers cool and freeze, thus releasing part of their saline content, which in turn increases the salinity of the subsurface waters (Jacobs et al., 1985). The densest waters (named High Salinity Shelf Waters—HSSW) are formed along the western sector of the Ross Sea and then move northward following the clockwise circulation (Budillon et al., 1999). These waters generally have temperatures close to the sea surface freezing point, between −1.95 and −1.75 °C, (Kurtz and Bromwich, 1983, 1985; Locarnini, 1994; Budillon and Spezie 2000) and salinity from 34.75 to 35.00, increasing with depth.

Part of these HSSW are known to move southward and flow under the Ross Ice Shelf, giving origin to a different type of water named Deep Ice Shelf Water (DISW, see Fig. 1) characterized by a low temperature (Jacobs et al., 1970). The average salinity of the DISW is about 34.62. This water mass spreads over much of the shelf break, where DISW are known to occupy the deeper layers of the water column, between 400 m and the bottom. Overlying this water mass, the Low Salinity Shelf Water (LSSW) fills the intermediate to subsurface layers (Jacobs et al., 1985).

Chlorofluorocarbon (CFC) concentration measurements in water masses which have circulated beneath the Ross Ice Shelf indicate that the evolution time from HSSW to DISW can be as short as 3–4 years. Trumbore et al. (1991), assuming that the DISW upwelling area is approximately 50 km^2 and, using an average outflow of ~ 1 cm s^{-1} as obtained by the HSSW/DISW concentration of CFC, found a DISW production rate of 0.5 Sv. Similar results were obtained in 1995 during the CLIMA cruise (Picco et al., 1999).

Mention must also be made of the presence of a front, the Antarctic Slope Front, (Jacobs, 1991). This is topographically controlled and interestingly is related to high biological productivity, being a source or sink region of heat, salt, nutrients, particulate, sediments and atmospheric gases (Trumbore et al., 1991). Temperature is the best indicator of its presence, showing gradients of 2–3 °C in only 20–30 km (Jacobs, 1991).

3. The data and their first treatment

During the austral summer 1994/1995, the CLIMA project of the *X* Italian Expedition carried out its first oceanographic cruise in the Ross Sea (January 7th to February 20th, 1995), collecting CTD casts and deploying current meter moorings. Note that only a subset of these data is analyzed here. Fig. 2 shows this working area, its bottom topography, the casts and the mooring positions. The CTD casts were performed using a Sea Bird Electronics SBE 9/11 PLUS coupled to a Carousel water sampler SBE 32. Also, oxygen and light transmission were measured.

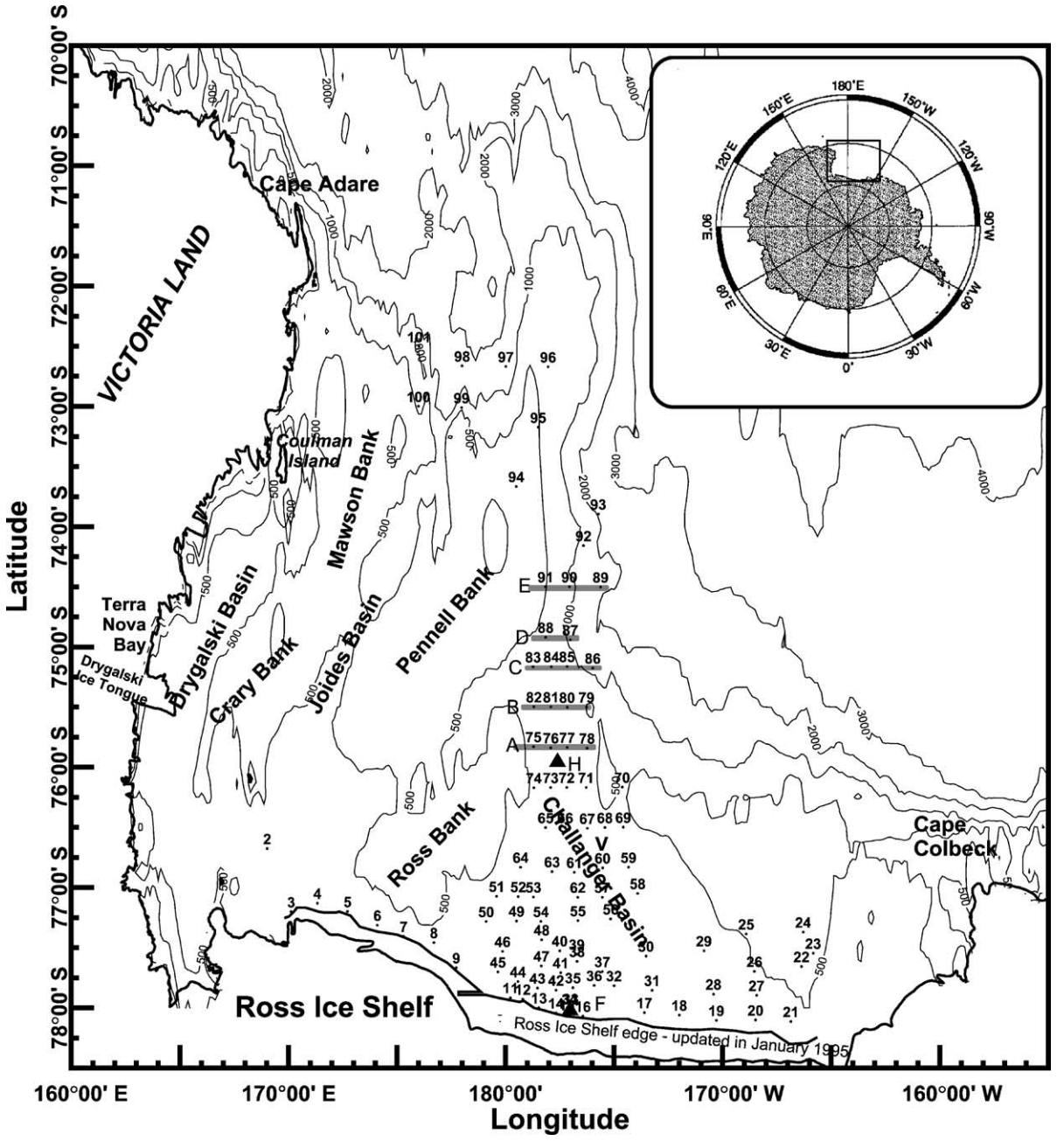

Fig. 2. General map of the Ross Sea with bottom topography in meters and geographical position of the CTD stations and of current meter moorings. Hydrologic properties of the transects A–E are discussed in the text.

Calibration of temperature and conductivity sensors were performed at the SA-CLANT CENTRE of La Spezia (Italy) before and after the cruise. The CTD was equipped with double temperature-conductivity sensors flushed at a constant rate. During the cruise, the CTD temperature was controlled by means of two

SIS RTM4200 digital reversing platinum thermometers. At every station, several samples of water at different depths were collected and analyzed on board using an Autosal Guildline Salinometer. According to the pre-and-after cruise calibrations, an offset of -0.0028 °C was applied to the raw temperature data. As to the conductivity calibration, only the bottom samples were used for the salinometer corrections. According to these data, an offset of 0.00095 S m^{-1} was applied to the raw conductivity data. Hydrological data were then corrected and processed according to international procedures (UNESCO, 1988). Standard algorithms (UNESCO, 1983) were used to compute derived quantities such as potential temperature, salinity, potential density anomaly.

The CTD stations 3 to 21 were distributed along the Ross Ice Shelf, with high resolution sampling. CTD stations 22 to 88 were $\sim$ 10 nautical miles apart, and distributed from the Ross Ice Shelf to the continental slope along the Challenger Basin, in order to detect the emerging area of the DISW beneath the Ross Sea and follow its spreading over the shelf break. They were located in zonal transects A, B, C, D and E (Fig. 2), placed $\sim$ 15 miles apart, centered on the observed core of the DISW. To investigate the processes occurring near the continental shelf break, where the CDW rises over the shelf, stations 89 to 101 were distributed between the shelf break and the open ocean.

During the same period, mooring $\tilde{H}$ was deployed in the central western part of the Ross Sea continental shelf and successfully recovered (Fig. 2) in order to evaluate more thoroughly the outflow of DISW beneath the Ross Ice Shelf, close to the continental slope. The layer investigated was essentially that between 230 m and the sea bottom. The mooring was equipped with different instrumentation, including current meters, temperature and conductivity sensors, sedimentary traps and turbidimeters. The current meters used were Aanderaa RCM7 or RCM8 models, while temperature and conductivity data were measured by SBE model SeaCat 16 and Aanderaa sensors. Current meters recorded data with a 1-h sampling frequency. A shift of 114° was assumed for the current direction in order to correct the local magnetic declination. To filter out semidiurnal and diurnal tides, as well as inertial oscillations, the data were low-pass filtered using a Chebyshev filter with a 50-h cutoff.

Particle presence was detected using a transmissometer to measure the attenuation of a red monochromatic light over a path length of 0.25 m. Each record was the result of an average of eight measurements, performed every 30 min.

4. Data analysis

Let us now consider the current meters deployed in this region; we will focus our attention on the mooring $\tilde{H}$ and on two of its four current meters, situated at depths of $\sim$ 500 and 600 m (Fig. 2). The currents observed at the mooring $\tilde{H}$ show a continuous northeastward outflow of water, probably coming from the eastern continental shelf and from the southern ice shelf.

More in detail, from an analysis of the data (Picco et al., 1999), the Ross Sea general circulation may be characterized by a period of low energy from March to June. The annual mean flow, at all depths, is directed towards northeast at velocities of 3–4 cm s^{-1}. The yearlong pattern is also characterized by frequent oscillations and two complete anticlockwise rotations occurring in July and January. For that part of the winter period which coincides with the cruise described herein, the average of the total velocity gives $\approx$ 7 cm s^{-1} for both the two deepest current meters, with high daily mean velocities (with peaks of more than 22 cm s^{-1}) directed mainly northeastward: the current field recorded at different depths of the water column shows a strong barotropic characteristic throughout the investigation period (February 1995 to January 1996).

In synthesis, the net annual mean flow, at all depths, is directed northeastward towards the shelf break, at velocities of 3–4 cm s^{-1}, indicating a constant outflow of DISW towards the open ocean, with peaks of more than 20 cm s^{-1}. Components of mesoscale activity (about 9 to 11 days), and other motions spread over a few days, were found in the current spectra at different depths. Water temperatures recorded in the near bottom layer (DISW) do not show any significant variability (Picco et al., 1999).

A set of low-pass filtered data is shown in Fig. 3a: from the beginning of February to the end of March (total of 40 days) currents are primarily in the first and second sector. Then, Fig. 3b gives both the light

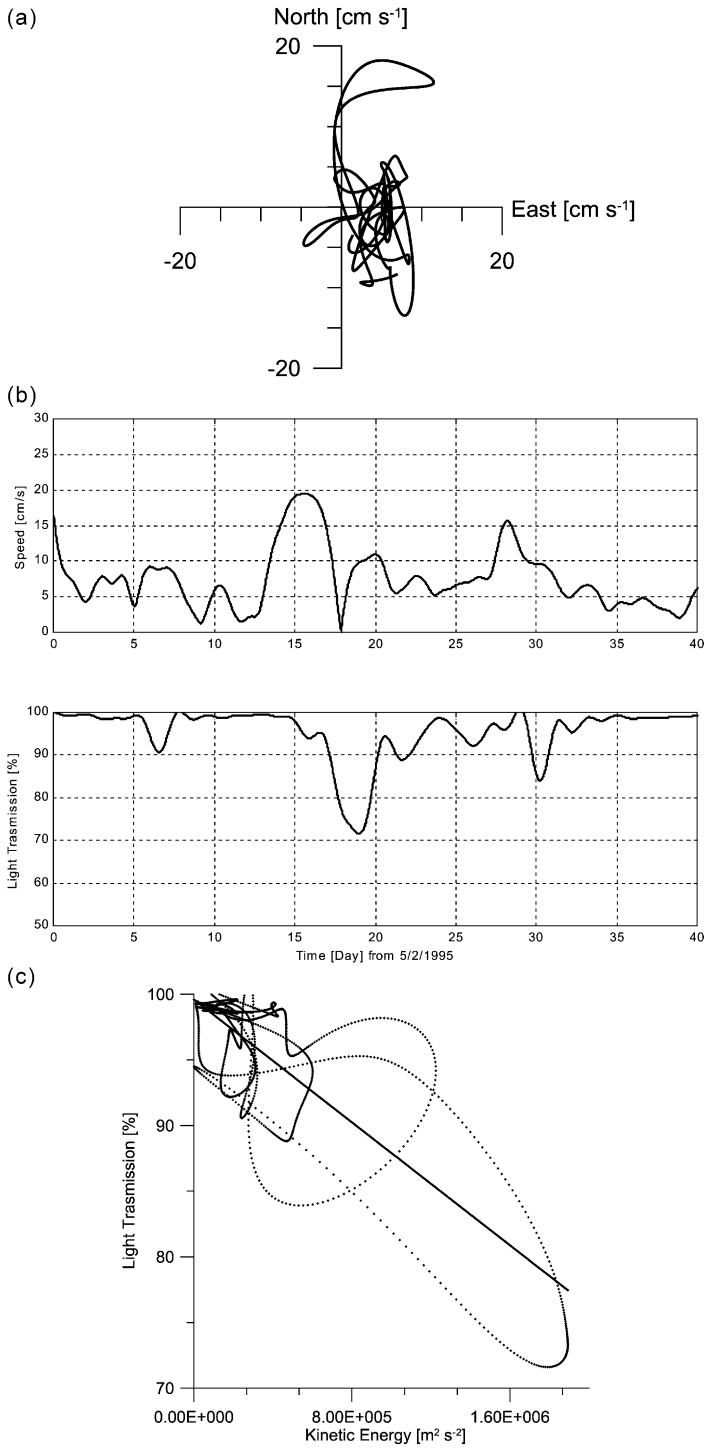

Fig. 3. (a) Near bottom current meter $\tilde{H}$ velocity (low-pass data) recorded during the first 40 day of working of $\tilde{H}$ (starting February 5, 1995). (b) Current water velocity and light transmission in the lowest layer of $\tilde{H}$ for 40 days. (c) Relation between the bottom water kinetic energy and light transmission for this observation period.

transmission and the bottom layer water velocity in this period of the observations. A rather unexpected correlation between these two quantities, with a time lag of 2.8 days, is evident, while observations in a longer period (1 year) do not show any such correlation. This time lag looks an intriguing physical quantity, probably related to air–sea interaction during the Austral summer. Finally it is of interest the relation between light transmission and the kinetic energy of the bottom water, showing for the largest velocity values an increasing trend (Fig. 3c). All this supports our model position, shown later in Eqs. (9) and (21). Indeed, Eq. (21) shows how the bottom stress can be reasonably schematized as being proportional to the bottom water velocity square, i.e. the kinetic energy, and also Eq. (9) postulates how the bottom light transmission, due to bottom particulate resuspension, is an increasing function of the bottom stress (Fig. 3c), a fundamental point for the following discussion.

The spatial DISW evolution can easily be described by means of vertical and horizontal sections of potential temperature. In order to reconstruct the thermohaline fields presented in the following, the kringing method has been used both for the vertical and horizontal sections. Kringing is a geostatistical method to grid data using appropriate variogram models. Moreover, an appropriate anisotropy ratio has been applied for both vertical and horizontal sections.

Since DISW is a water mass characterized by temperature below the surface freezing point, for each station in the central Ross Sea, the maxima of the difference between the potential temperature and the surface freezing point were also analyzed. This horizontal distribution (at depths varying from 350 m close to the Ross Ice Shelf to 500 m) is in Fig. 4. The pathway of the DISW is relatively clear: maximum temperature values indicate that most of the current follows the bathymetry of the shelf, and also the nonhomogeneous dilution of the DISW during its northward motion is evident.

We can now analyze in more detail the information relative to the various hydrological transects.

Transect A—Stations 75–78, 2 February. A very dense water (essentially DISW with $\sigma_\theta > 27.90$) is evident over the sea bottom from $\sim$ 450 to $\sim$ 600 m depth. From current meter data relative to mooring $\tilde{H}$ and the vertical section of Fig. 5, we see that DISW flows northward, under a $\sim$ 200-m-thick layer of LSSW ($\sigma_\theta \sim 27.82$–27.95), at a velocity $\sim 7\ \mathrm{cm\ s^{-1}}$.

Transect B—Stations 79–82, 3 February (Fig. 5a). From the analysis of the isopycnals, as in transect A, very dense water with $\sigma_\theta \sim 27.95$–27.99 occupies the deepest levels of stations 81–79 with values of potential temperature θ and salinity S intermediate to those of HSSW and DISW, namely $\theta \sim -1.94\ ^\circ\mathrm{C}$ and $S \sim 34.74$–34.76. The θ and S characteristics of the deep layers of this transect are similar to those of transect A. Note how the bottom layer velocity looks larger than the upper LSSW layer velocity.

Transect C—Stations 83–86, 3 February. In this transect, the Antarctic Slope Front is visible at station 85. A northward flow is evident on the eastern boundary of the section (station 86), where a warm water mass ($\theta \sim 0.4\ ^\circ\mathrm{C}$) is also present. The maximum $\sigma_\theta \sim 27.98$ is visible only in the bottom layers, with θ and S similar to those of transects A and B.

Transect D—Stations 87–88, 3–4 February. The maximum value of σ_θ is ~ 27.91 in station 88. Salinity values are smaller than those found in other transects, about 34.66. Over the shelf, θ continues to be near $-1.85\ ^\circ\mathrm{C}$, but on the deeper side of this transect, it increases, as in station 86 of transect C. Between the surface and the level of 250 m depth, one can observe an inversion of the slope of the isopycnals, thus revealing a baroclinic velocity between the surface layers and the bottom current.

Transect E—Stations 89–91, 5 February (Fig. 5b). Very different hydrologic characteristics are observed in this zone, producing a distinct density field. The density profiles show a maximum value of 27.82–27.84 on the shelf bottom up to 600 m (stations 91–90). There is again an inversion of the slope of isopycnals in the upper layer with respect to the deep waters, which are separated at a level of $\sim$ 200 m. Also θ, between -0.8 and $-1.1\ ^\circ\mathrm{C}$, is higher than in the first two transects: station 89 has more or less the same thermohaline characteristics as those already observed in the outer part of the other transects. Salinity presents somewhat lower values than the other transects, namely ~ 34.6–34.7.

Of particular importance are potential temperature, salinity and light transmission data in the near bottom layer, shown in Fig. 6. These data are expressed in arbitrary units and are to be considered as a qualitative comparison of the light transmission behavior with S

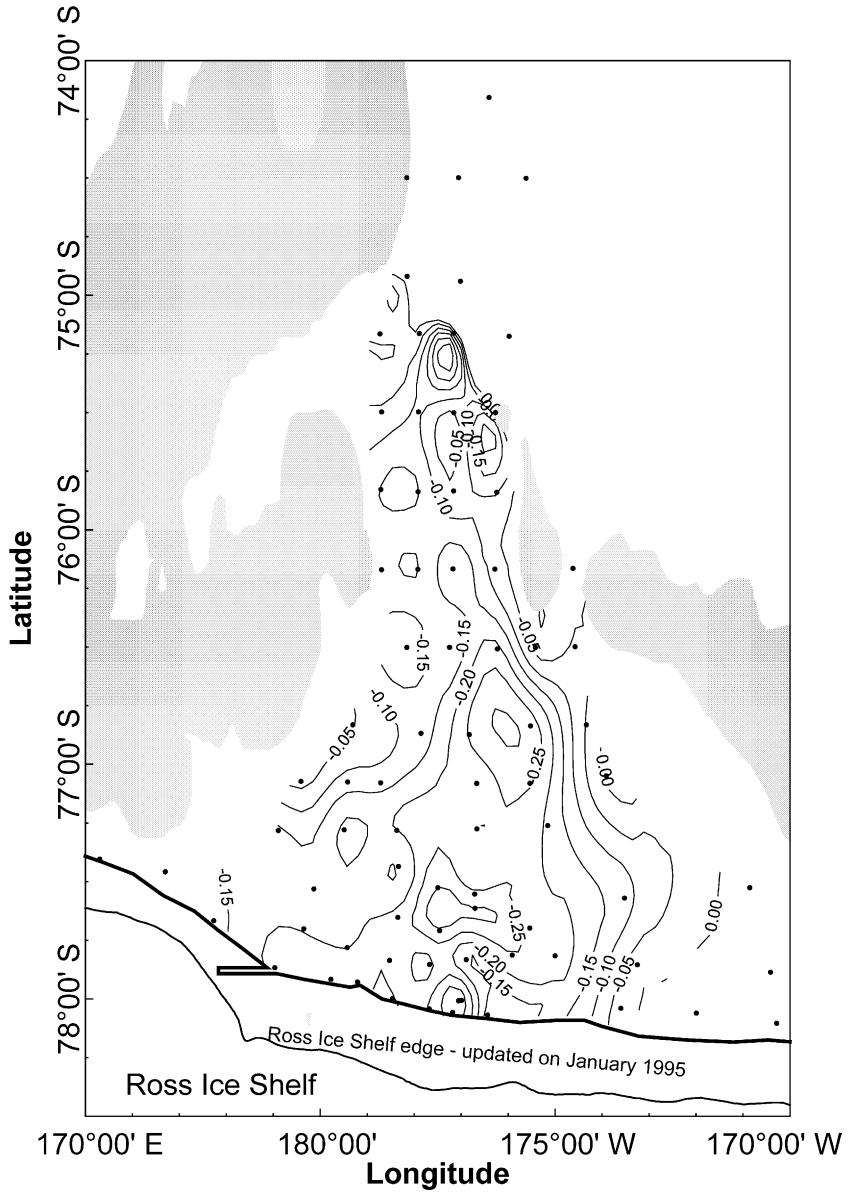

Fig. 4. Horizontal distribution of the maximum temperature anomaly calculated by the difference between the (in situ) potential temperature and the surface freezing point. Dots indicate the position of the casts used to contour the data. Shaded area indicates a shelf shallower than 500 m.

and θ, along the vertical. Stations over the continental shelf are characterized by a bottom layer of 50–100 m, showing an impressive sudden change of salinity, potential temperature and values of light transmission. This is the most evident signature of the presence of a turbulent bottom current, where the water is noticeably mixed with bottom particulate.

It is noteworthy that similar decrease in light transmission is not observed at the stations of transect E, where, indeed, the DISW disappears abruptly, over the continental shelf (station 90) nor outside the shelf break (station 89). Recent studies showed that the motion of DISW close to the bottom layer in this area is strongly related to an increase of particulate matter. Actually,

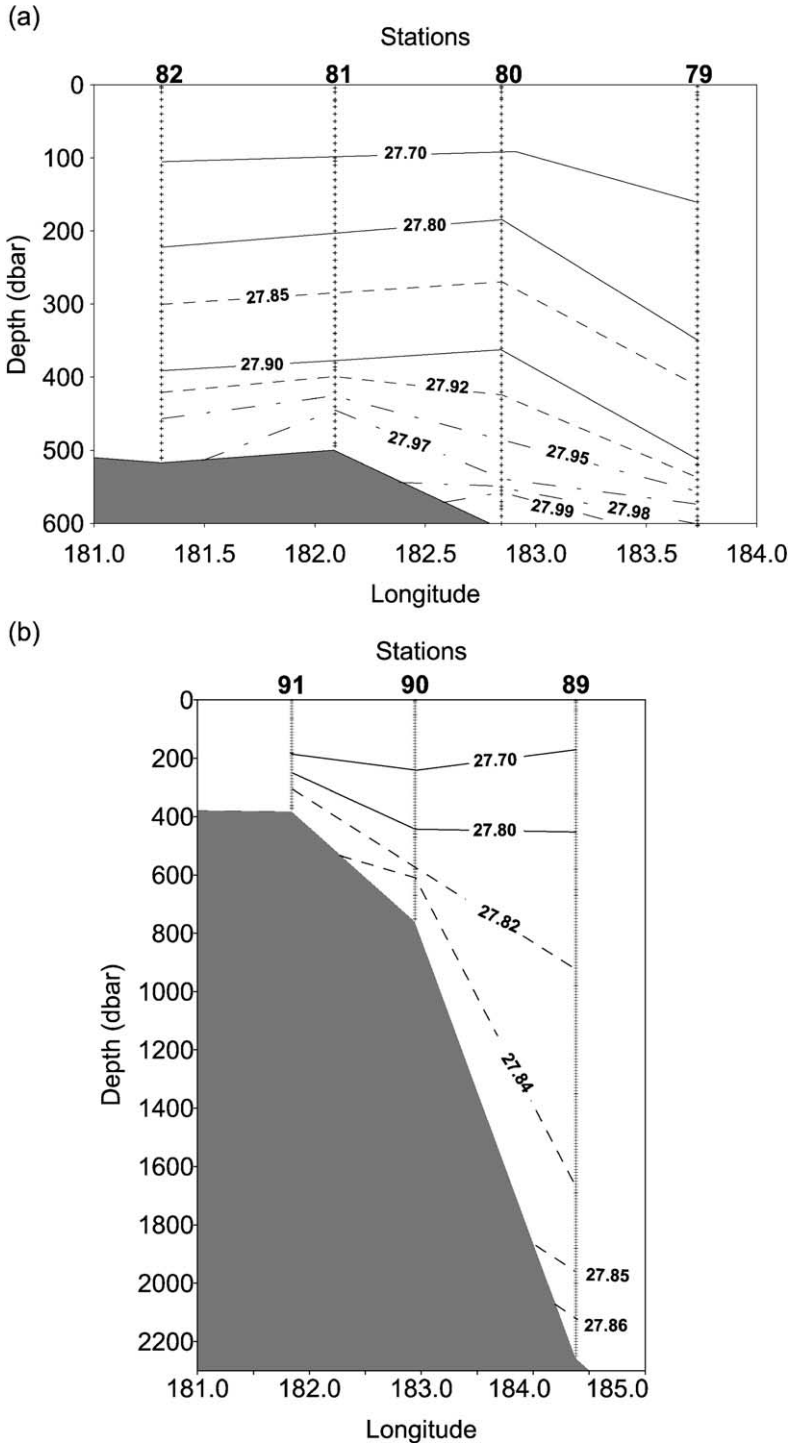

Fig. 5. (a) Vertical section of σ_θ for transect B, as shown in Fig. 2. We have chosen as boundary between bottom Deep Ice Shelf Water (DISW) and the upper layer of Low Salinity Shelf Water (LSSW) the value $\sigma_\theta = 27.95$, while LSSW has an upper boundary at $\sigma_\theta = 27.82$. (b) Vertical isopycnal of transect E. All the definitions are as for transect B.

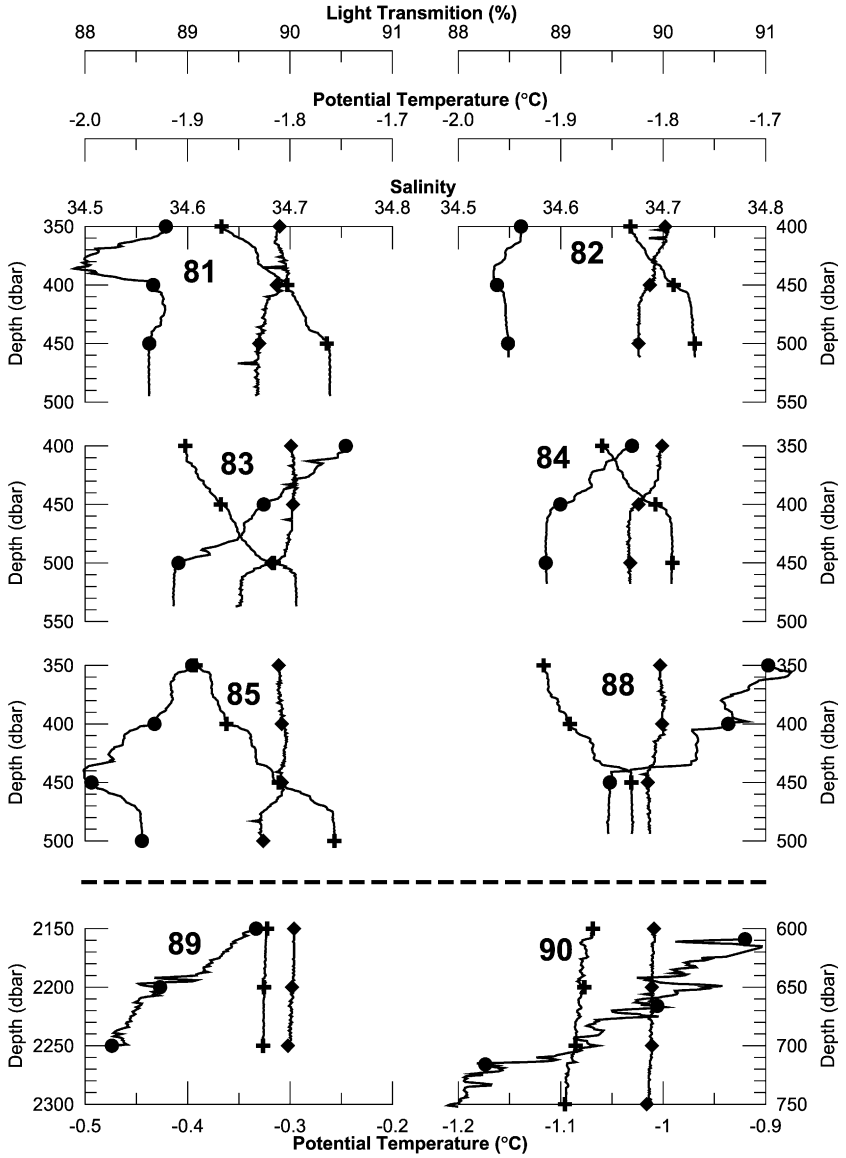

Fig. 6. Potential temperature (dots), salinity (crosses) and light transmission (arbitrary units, squares) data versus depth for various stations over and outside the continental shelf. Note the different temperature ranges for stations 89 and 90.

Tucci et al. (1999) have estimated the correlation between the DISW and the presence of the particulate matter larger than 60 μm; they measured a steady increase of 8% of the particulate matter in the bottom layer which was attributed to resuspension phenomena. This has been also confirmed by the higher size values, not detected in the upper layers (Tucci et al., 1999). Thus, the presence of the DISW over the Ross Sea continental shelf is related to a significant presence of particulate, either of biological or geological origin.

5. Some fundamental questions

The dynamics of the very dense water (DISW) observed over the shelf in its flow towards the north

deserves some discussion. Indeed, this very dense water ($\sigma_\theta \sim 27.95–27.99$) fills the water column from 450 m down to the shelf bottom (nearly 600 m depth) in transects A, B and C. However, further north, in transect D, the water with σ_θ greater than 27.91 on arriving at transect E seems to disappear, since only water with $\sigma_\theta \sim 27.82$ remains over the shelf.

Horizontal potential temperatures, in comparison with the surface freezing point (Fig. 4), allow an explicit comparison between these shelf waters and those found downslope and show in detail the evolution of the hydrological characteristics of the DISW in its northward motion. In addition, from Fig. 7, one can analyze the different $\theta–S$ diagrams from the Ross Ice Shelf (station 15) as far as the open ocean (station 89). This is quite important since we know that density currents over a realistic slope, such as these dense shelf waters, follow topographic contours at almost constant depth in a geostrophic motion, with relatively

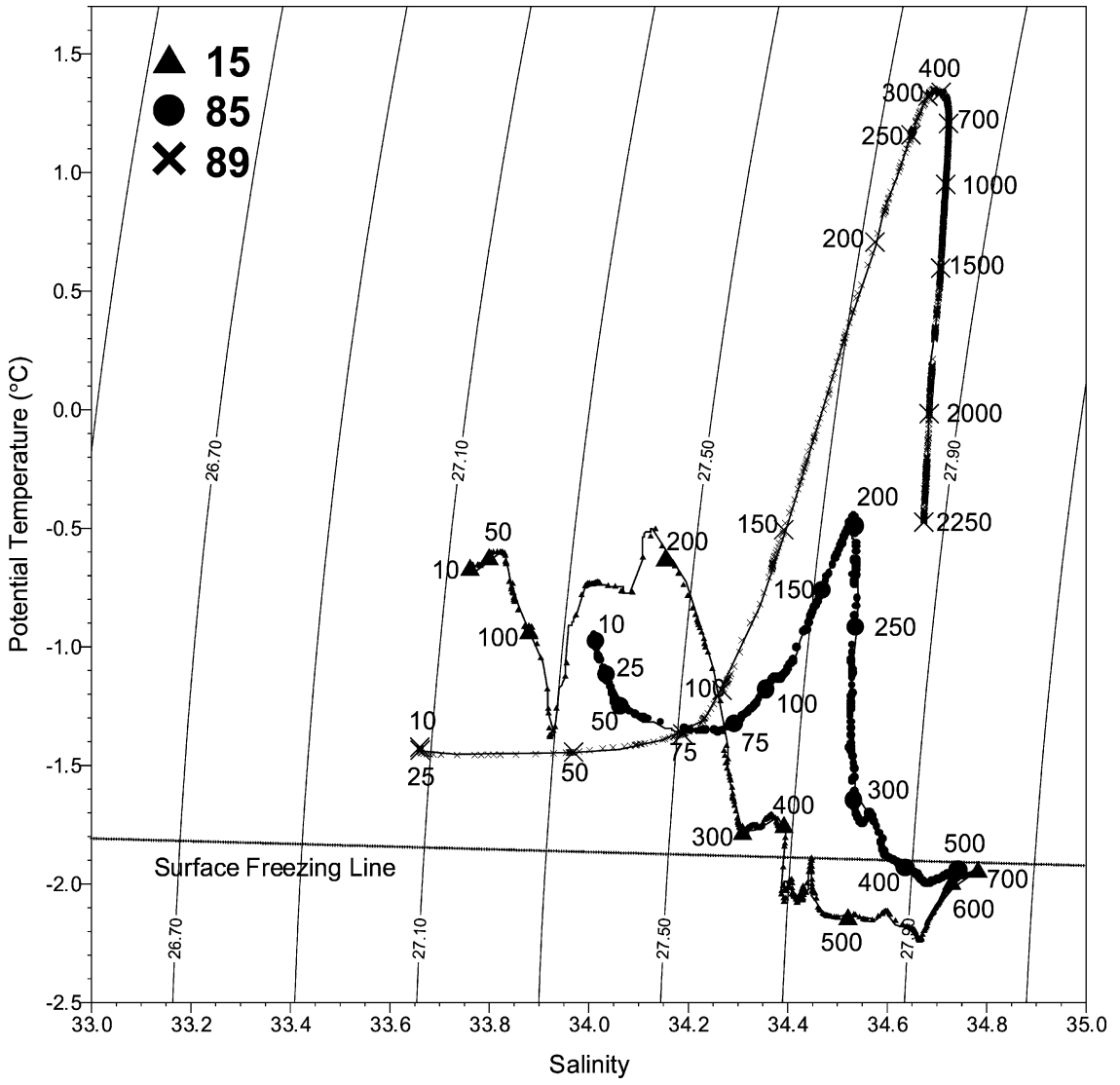

Fig. 7. Synthetic $\theta–S$ diagrams for station 15 (triangle) near the Southern boundary of the Ross Sea, of station 85 (circle), and station 89 (cross).

constant shape and velocities (Smith, 1975; Emms, 1997; Baringer and Price, 1997). Conversely, from our data, we see that this particularly cold dense water disappears and thus one is led to investigate the mechanisms responsible for this intriguing sinking process.

There are several models that can give some insight into the dispersion of the bottom current evident in these observations. To investigate turbulent mixing, the classical elementary mechanisms are shear instabilities, Kelvin–Helmholtz instabilities and baroclinic instabilities, which are mostly related to differences in seawater hydrological characteristics and/or between the current velocities (Drazin and Reid, 1981; Pedlosky, 1979). None of there mechanisms would however give sediment evolutions as those shown in Figs. 3 and 6.

So also other effects must be considered: first, density current flowing over a regular slope can be deflected by pressure gradients due to more superficial flows, for instance, if a more vigorous parallel surface current pushes the bottom current offshore far from the shelf (Astraldi et al., 2001), towards a deeper level. Second, if the sea bottom is not regular but is intersected by a sharp marine canyon, then the density current can give rise to a violent turbulent sinking and flattening evolution, down to the deepest marine layer. This has been studied in a classical tank experiment by Sugimoto and Whitehead (1983), in field observations of the Weddell Sea (Killworth, 1983) and also in the Adriatic Sea (Bignami et al., 1990). In addition, it is also possible that some external forcing or hydrodynamic instability processes can perturb the bottom particulate that mixes with the bottom current. The consequent density increase perturbs the bottom current, thus producing a steady kind of turbidity current (Caserta et al., 1990; Salusti, 1996). These rather theoretical questions will be examined in the following sections.

6. Geostrophic and ageostrophic density currents in marine channels and straits

In the light of the preceding discussion, we shall now discuss stability properties of a bottom current flowing steadily along a regular marine bottom $b(x,y)$ such that $(\partial b/\partial x) \ll (\partial b/\partial y)$, where $x(y)$ is the along-channel (cross-flow) coordinate (Fig. 8): this could be

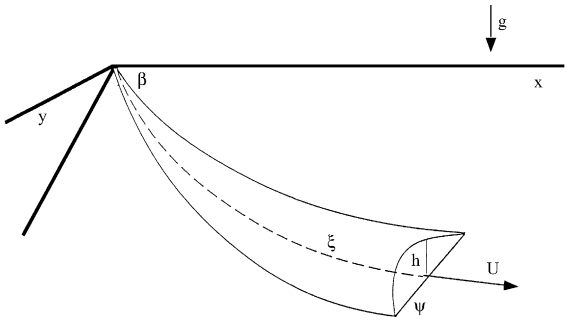

Fig. 8. General view of the density current flow along a regular slope in the Southern hemisphere, with alongflow velocity U, thickness h, alongstream (cross-stream) coordinate $\xi(\psi)$. Note that β, the deflection angle between x and ξ, is generally very small even if in this drawing it has been exaggerated for the sake of clarity. The sea surface coordinates are x and y.

the case of a strait, a channel or even a submarine channel.

As far as the dynamics of the lowest layer are concerned, a steady model that parallels recent studies by Emms (1997) and Baringer and Price (1997) on density currents in a still environment will be discussed in the following. We consider equations related to incompressibility, downstream momentum and across-stream momentum for a steady flow, although not under still layers but under, say, steady currents with velocities V_i along the channel. In greater detail, the bottom current is assumed to be symmetrical about its centerline along the streamwise coordinate ξ, and with across-stream coordinate ψ (Fig. 8). Indeed, the model equations are derived by introducing a transformation in a streamwise coordinate system (ξ,ψ) that forms a deflection angle β with the usual (x,y) coordinates, and then space-averaging over a cross-section of the current (Smith, 1975).

If the height of the bottom current is called $h(\xi)$ for the sake of simplicity, as the alongvein fluid velocity is $U(\xi)$, incompressibility gives (Smith, 1975):

$$\frac{\partial}{\partial \xi}\int\int U\,\mathrm{d}z\mathrm{d}\psi = \frac{\partial}{\partial \xi}\int hU\,\mathrm{d}\psi = \frac{\partial}{\partial \xi}(\mathscr{A}U) = \mathscr{E}$$
$$= \int \mathscr{E}^* \,|\, U - V \,|\, \mathrm{d}\psi = \mathscr{E}^* \,|\, U - V \,|\, W \qquad (1)$$

the value of the current being averaged over a cross-section. Here, V is synthetically the immediately upper layer velocity, $\mathscr{A} = \int h\mathrm{d}\psi \simeq hW$ is the bottom current

cross-sectional area, W is the current width and $\mathscr{E}$ represents the total entrainment between the dense cold current and the upper layer, an effect discussed at length by Ellison and Turner (1959) and Turner (1986).

Denoting for the sake of simplicity the dense current density as ρ (ξ), conservation of mass gives (Smith, 1975):

$$\frac{\partial}{\partial \xi}\int\int U\rho \mathrm{d}z\mathrm{d}\psi = \frac{\partial}{\partial \xi}(\rho \mathscr{A} U) = \rho_0(z)\mathscr{E} = \rho_0(z)\mathscr{E}^* \mid U - V \mid W \tag{2}$$

where $\rho_0(z)$ is the local environmental density, eventually depending on the depth z. Similar relations hold for any tracer present in the seawater.

The downstream nonlinear steady momentum is assumed to be balanced by frictional effects and the hydrostatic pressure gradient. Thus, the conservation of volume (1), together with that of momentum, gives

$$\begin{aligned}\frac{\partial}{\partial \xi}\int\int \mathrm{d}\psi \mathrm{d}z(U^2 + g'\,[b+z]) &= \frac{\partial}{\partial \xi}\left(U^2\mathscr{A} + g'\,\mathscr{A}\left[b+\frac{h}{2}\right]\right)\\ &= \mathscr{D} + F - f\int\int \mathrm{d}z\mathrm{d}\psi V\sin\beta\\ &= \mathscr{D} - fV\mathscr{A}\sin\beta + F\end{aligned} \tag{3}$$

where $\mathscr{D}$ is the total bottom drag, $g' = g(\rho - \rho_0)/\rho_0$ is the relative buoyancy and F is the alongflow component of external forcings. Note that incompressibility and alongstream momentum give the first term in Eq. (3). The second term of Eq. (3) is the baroclinic pressure term, which accounts for changes in the hydrostatic pressure due to variations in the depth of the interface. About the external forcings, there is no restriction in theory. In practice, this F could be given by quick transients in the pressure field, the result of upper layer currents variations, storms, trains of internal waves or also sharp variations of the sea bottom that can give origin to confluence of currents or to hydrodynamic current perturbations. At great depths, this last type of topographic forcing is probably the most effective in deflecting bottom currents.

Finally, we equate the effect of the cross-stream component of gravity perpendicular to the direction of flow, upper layer hydrostatic pressures and the Coriolis force to give

$$U^2\partial\beta/\partial\xi + fU + \frac{\partial}{\partial\psi}[g'(h+b)] = fV\cos\beta + F^* \tag{4}$$

where F^* is the cross-flow component of external forcings. Note the presence of an unusual pressure gradient term in this equation (Emms, 1997) and also the term $fV\cos\beta$, synthesizing the pressure effect of the steady currents flowing over the vein (Appendix A). It has to be added how in Eqs. (1)–(3) and also in Eq. (4) we describe currents in a strait or in a channel, while in open sea these terms are more complex, in particular $fV\cos\beta$ in Eq. (4) cannot be so easily simplified.

We will now focus our attention on incompressibility and conservation of momentum, namely

$$\frac{\partial}{\partial\xi}(\mathscr{A}U) = \mathscr{E}^* \mid U - V \mid W$$

$$\frac{\partial}{\partial\xi}(U^2\mathscr{A} + g'\mathscr{A}[h/2+b]) - \mathscr{D} + fV\mathscr{A}\sin\beta = F$$

$$U^2\frac{\partial\beta}{\partial\xi} + f(U - V\cos\beta) + g'\frac{\partial}{\partial\psi}[h+b] = F^* \tag{5}$$

while Eq. (2) will be used in the following to estimate the entrainment. Note how, since $(\partial b/\partial x) < (\partial b/\partial y)$, for small β, we have

$$\frac{\partial b}{\partial\psi} \simeq \frac{\partial b}{\partial y}\cos\beta \sim \frac{\partial b}{\partial y}[1 + \partial(\beta^2)] \sim \frac{\partial b}{\partial y} \tag{6}$$

since the error, of the order of β^2, has to be very small. This finally gives our main equations

$$\frac{\partial}{\partial\xi}(\mathscr{A}U) = \mathscr{E}^* \mid U - V \mid W$$

$$\frac{\partial}{\partial\xi}(U^2\mathscr{A} + g'\mathscr{A}[h/2+b]) - \mathscr{D} = F$$

$$U^2\frac{\partial\beta}{\partial\xi} + f(U - V) + g'\frac{\partial}{\partial y}[h+b] = F^* \tag{7}$$

Note how disregarding centrifugal effects, which in any case are proportional to U^2, the third equation becomes a simple geostrophic relation.

These model equations are classical (Emms, 1997; Baringer and Price, 1997), but here the effect of moving overlying layers is considered through the presence of the immediately upper layer velocity V. An important point is that Eqs. (2) and (3) can be seen as describing a one-dimensional space process on $h(\xi)$ and $U(\xi)$, while β appears only in Eq. (4) as a function of ξ and ψ. However, this is only partially true since (F,F*) and b are actually functions of both ψ and ξ, and so these equations can be rigorously decoupled only for regular F and b or, more interestingly, for an extremely sharply localized type of F and b. From the third of Eq. (7), it is evident that the current can be deflected, i.e. the angle β can be changed only by variations of V, g' or b, at least as long as U and h remain fairly constant.

These considerations allow us to obtain a different insight into dense water dynamics. First, if the upper layer velocity V increases, this corresponds to a deflection of LSSW, or also CDW, towards West. Consequently, the DISW is pushed eastward and necessarily sinks to deeper layers because of its high density. One may however object that DISW disappears even when the effect of LSSW or CDW is not so strong, suggesting that this is probably not the only important deflecting mechanism, in addition not concerning bottom particulate as evident in Fig. 6.

One can also investigate the effect of a certain variability of bottom topography b since it is well known that if a density current flowing geostrophically over a shelf, or even a shelf break, intersects an offshore oriented marine canyon, then its geostrophic flow is interrupted and a downflow of dense water along the canyon occurs (Killworth, 1983). Indeed from Eqs. (5) and (7), it is evident that abrupt changes of b can formally act as an external force. A particularly clear reproduction of this deepening has been obtained in the classical tank experiment of Sugimoto and Whitehead (1983). It must be however added that this is not a total disappearance since also downstream from the canyon some dense water is still observable over the shelf, both in tank experiments and in field observations (Bignami et al., 1990). Also, this mechanism does not involve bottom particulate.

As regards (F, F*), it is clear that at such depths external forces do not have any great importance, but current instabilities or also a current–bottom particulate interaction can raise some bottom particulate and thus increase the seawater's effective density. Indeed, we know from the current meter $\tilde{H}$ data set that although the bottom velocities were often as small as ~ 3–4 cm s^{-1}, some intense peaks as high as 22 cm s^{-1} were observed during the cruise. It is thus possible that such velocity peaks, in a well-localized geographical region, give rise to a strong interaction with the sea bottom particulate and thus a density-turbidity current develops (Salusti, 1996). In such a case, one can expect that a larger space-scale flow originates, transporting the DISW far deeper. Note also that such an effect corresponds formally to a dramatic increase of g' in the third of Eq. (7). Finally, it is possible that the situation evolves as a classical impulsive turbidity current if a large amount of bottom particulate is present. One can however also imagine that for a small amount of available bottom particulate, in a sort of equilibrium with that carried by peaks of the bottom current, a different slowly evolving density-turbidity current finally emerges.

7. Turbidity effects

To fully discuss the last instability effect, namely current–bottom particulate interaction, the motion of a slightly viscous dense fluid carrying uniform noncohesive sediment with "fall velocity" v_s, which is free to exchange with similar sediment on the sea bottom, is analyzed here. More specifically, the motion of a slightly viscous dense fluid of density ρ over a regular slope, below a lighter fluid of density $\rho_0(z)$, is now theoretically discussed. Here, ξ and z are the alongslope and vertical coordinates (Salusti, 1996). The upper fluid is now assumed to be at rest. Let us stress that $\rho>\rho_0(z)$ both for the entrainment of bottom particulate and for an initial density difference Δ due to the hydrological characteristics of the oceanic water masses.

To treat these equations, one needs detailed information on sediment dynamics, namely on a field for which today so much experimental data are available that a clear synthesis is difficult to attain. In particular, in recent interesting studies by Parker et al. (1986) and Stacey and Bowen (1988a,b), the system time-evolution is described in detail, but the ultimate equations are so complex that either time or one space dimension has

to be disregarded. This encourages a more synthetic approach: Caserta et al. (1990) recently proposed a heuristic model of a slowly varying density current flowing down a bottom slope Θ and raising some bottom sediment: the density $\rho > \rho_0 + \Delta$ is assumed to vary only as a result of the shear stress on the sea bottom, since it is this stress that raises the bottom sediment and governs its resuspension/deposition. So, following an old idea of Plapp and Mitchell (1960), this effect is assumed to be a sensitive function of the bottom stress, i.e. of

$$\tau = \nu\rho \left.\frac{\partial U}{\partial z}\right|_{z=0} \tag{8}$$

minus a term proportional to the sediment fall velocity v_s, where ν is the friction coefficient.

Following these ideas through, if a quantity of suspended sediment is formed and quickly redistributed uniformly in the whole thin turbulent density current, the resulting density ρ can be represented as

$$\rho - \rho_0 - \Delta = \frac{q_0}{h} e^{\frac{\tau-\tau_0}{\tau_0}} \qquad \tau_0, q_0 = \text{constant} \tag{9}$$

heuristically assuming an exponential behavior for the bottom shears (Caserta et al. 1990). These constants are discussed in Salusti (1996). One point deserves attention: this relation (9) is clearly valid as long a very large amount of bottom particulate is present. In reality, this idealization holds for short-time phenomena; if however one wants to investigate long-lasting events ruled by a quasi-steady balance of bottom sediments, one has to take into account the global balance of bottom sediments. This results in a particularly difficult nonlinear equation. In formulae, this could mean that q_0 is not really a constant but depends on the previous history of the bottom sediments. More simply, one can say that $q_0(t)$ is a very slowly time-dependent function that initially is q_0, and then decreases over large time scales.

It is of some interest to compare Eq. (9) with the results of Stacey and Bowen (1988a,b) describing the density evolution of impulsive turbidity currents, namely

$$\rho - \rho_0 = \rho - \rho_0|_{\text{sea bottom}} = \exp\left\{-v_s \cos\Theta \int_0^z \frac{\{1 + B_2 R_i\}^{1+\gamma}}{\nu_0} dz\right\} \tag{10}$$

where γ, B_2 are suitable constants, R_i is the Richardson number and ν_0 is the eddy viscosity for unstratified fluids. All this shows that it is not an easy task to fully compare our schematic assumption (9) with those discussed in the literature. Intuitively, this model can be considered valid if the sediment is so fine-grained and light as to be dispersed immediately inside the thin turbulent bottom flow.

In order to investigate the effect of such a water–particulate interaction on the density current stability, note how in Eq. (7) the Coriolis force does not appear in the alongflow momentum equation. So, in practice, we are dealing with a one-space dimensional flow over a regular slope Θ, even if to discuss these instabilities the time must be explicitly taken into account in the original set (7). A perturbative approach is thus possible, with $h(\xi,t) = h_0(\xi) + h'(\xi,t)$ and $g' = g(\Delta\rho/\rho) \equiv \Gamma_0(\xi) + \Gamma'(\xi,t)$, $h_0(\xi)$ and $\Gamma_0(\xi)$ being the unperturbed steady values.

Such modelling involves computing the bottom stress due to both the quasi-steady current and its short space-scale perturbation. So inserting the stress-dependent density (9) in the alongflow momentum (7), after some computations (Salusti, 1996), one obtains

$$\frac{\partial^2 h'}{\partial t^2} = \Gamma_0 h_0 \frac{\partial^2 h'}{\partial \xi^2} + g\epsilon \frac{h_0}{2} \frac{\partial^3}{\partial \xi^3} h'^2 + \nu \frac{\partial^2}{\partial \xi^2} \frac{\partial}{\partial t} h' - \frac{1}{4t^*} \frac{\partial}{\partial t} h' + h_0 \frac{\partial F}{\partial \xi} \tag{11}$$

where

$$\epsilon = \frac{1}{g} \frac{4\Gamma_0^2 \varrho_0 h_0 (1 - e^{\frac{-t}{4t^*}})}{\pi^2(\tau_0 - \Gamma_0 \rho_0 h_0 \Theta)} \simeq \frac{4}{g\pi^2} \times \left.\frac{\Gamma_0^2 \rho_0 h_0}{(\tau_0 - \Gamma_0 \rho_0 h_0 \Theta)}\right|_{t/t^* \sim \mathcal{O}(10)} \partial \sim (-1, -0.1)$$

The fundamental role of the "ignition time" $t^* \equiv h^2{}_0/\pi^2\nu$ will become clear in the following, while the physical meaning of ε as a dimensionless coefficient related to nonlinear effects emerges naturally.

We first discuss the steady case. If F can reasonably be considered time-independent, then Eq. (11), with $\partial/\partial t = 0$, describes cases of considerable interest. If a steady F has a local origin, as for example schematizing the effect of a sharp bottom irregularity, we can say that $F = F(\xi)$ for $-a < \xi < a$, i.e. the region

where the perturbation is strong. The current steady evolution is thus given by

$$\Gamma_0 h_0 \frac{\partial^2}{\partial \xi^2} h' + g \frac{\epsilon}{2} h_0 \frac{\partial^3}{\partial \xi^3} (h')^2 + h_0 \frac{\partial}{\partial \xi} F = 0 \qquad (12)$$

Integrating twice and assuming that, before the region with such an irregular sea bottom $h'=0$ then Eq. (12) becomes

$$\Gamma_0 h' + g \frac{\epsilon}{2} \frac{\partial}{\partial \xi} (h')^2 + \int_{-a}^{\xi} F(\xi') \mathrm{d}\xi' = 0 \qquad (13)$$

with $\epsilon < 0$. This is a much simpler ordinary nonlinear equation: if $\epsilon \equiv 0$, i.e. no sand–water interaction is considered and

$$\Gamma_0 h' = -\int_{-a}^{\xi} F \mathrm{d}\xi' < 0 \qquad (14)$$

due to the intuitive fact that if an external force accelerates the fluid then because of the continuity, h becomes smaller. However, if $\epsilon \neq 0$, then near $\xi = -a$ one has that $h' \sim 0$ and so

$$\Gamma_0 h' + \int_{-a}^{\xi} F \mathrm{d}\xi' = -g \frac{\epsilon}{2} \frac{\partial}{\partial \xi} (h')^2 \qquad (15)$$

which implies

$$h' \simeq \sqrt{-\frac{2}{g\epsilon} \int_{-a}^{\xi} \mathrm{d}\xi' \int_{-a}^{\xi'} F(\xi'') \mathrm{d}\xi''} > 0 \qquad (16)$$

In the general time-dependent case, Eq. (11) is a complex nonlinear diffusive equation; its treatment in some cases reveals pathologies, such as an explosive steepening of the signals (Whitham, 1974). A numerical solution cannot consequently be considered fully satisfactory. So let us first discuss some simpler cases: if $\epsilon = 0$, the dynamic effect of bottom entrainment vanishes quickly, so the bottom layer dynamics is driven only by the hydrological density difference Δ. After some time, ϵ can no longer be considered nil, so one is led to investigate perturbative solutions of Eq. (11) in ε and v such as

$$\begin{aligned} h' &= h'(\xi - \mathscr{V} t, \epsilon t) \equiv h'(y, \epsilon t) \text{ with } y \equiv \xi - \mathscr{V} t \\ &= \xi - t\sqrt{\Gamma_0 h_0} \end{aligned} \qquad (17)$$

Using the following substitution for the function ϕ and the new "time" η, namely $\mathrm{e}^{-\frac{\pi^2 \nu t}{8\epsilon h_0^2}}$ that gives

$$\begin{aligned} &h'(y,t) - \frac{\nu \mathscr{V}}{\epsilon h_0 g} \\ &\quad = \mathrm{e}^{-\frac{\pi^2 \nu}{8\epsilon h_0^2} t} \phi\left(y, \mathrm{e}^{-\frac{\pi^2 \nu}{8\epsilon h_0^2} t}\right) \equiv \eta. \quad \phi(y,\eta) \end{aligned} \qquad (18)$$

all this finally becomes (Salusti, 1996)

$$\begin{aligned} &\frac{\pi^2}{4h_0^2} \frac{\partial}{\partial \eta} \phi - \frac{\epsilon h_0 g}{\nu \mathscr{V}} \frac{\partial}{\partial y} \left\{ \phi \frac{\partial}{\partial y} \phi \right\} \\ &\quad + \nu \frac{\pi^2 \nu}{4h_0^3 \epsilon} \frac{1}{\eta} + F = 0 \end{aligned} \qquad (19)$$

In general, Eq. (19) may be said to allow investigation of the effect of both space and time variation on current evolution, while the vertical variability is schematized as a two-layer system. Solutions of Eq. (19), a nonlinear heat type, can be grasped intuitively by analyzing the function ϕ. In fact, if $\phi > 0$, then everything is as is normally the case in diffusion equations, but if $\phi < 0$ everything is as in the case of $\phi > 0$ but with an inverted time $\eta \rightarrow -\eta$: in this second case, the solutions grow exponentially in a particularly dramatic way, much quicker than the usual exponential behavior of hydrodynamic instabilities, and catastrophic events are to be expected. This corresponds mathematically to the quantity $h' - (v\mathscr{V}/\epsilon h_0 g)$ changing sign and allows to gain some insight into the classical "ignition point" of the impulsive turbidity currents, at least from the hydrodynamic stability viewpoint.

In synthesis, the frictional terms give a general space-time damping, as one would expect. Conversely, the nonlinear term proportional to ϵ can lead to explosive behavior: since h' is an oscillating perturbation, the quantity

$$h' - h^* \equiv h' - \frac{\nu \mathscr{V}}{g \epsilon h_0} = h' - \frac{\pi^2 \nu (\tau_0 - \rho_0 \nu^2 \Theta)}{4\nu^3 \rho_0 (1 - \mathrm{e}^{\frac{-t}{4t^*}})} \qquad (20)$$

is consequently a critical quantity. This means that if $h' > h^*$, due to the effect of some external forcings, then the system is no longer stable. In such a context, the factor $(1 - \mathrm{e}^{-t/4t^*})$ contained in Eq. (20) gives a kind of "time delay" of considerable mathematical

interest: for $t \sim 0$, one has that $h^* \rightarrow \infty$ and so any transient forcing gives rise to perturbations that cannot grow. Consequently, the system returns naturally to the original situation of a density-driven current. However, if the perturbation lasts long enough, roughly $\sim 10t^*$, then the nonlinear terms become important and eventually generate ignitions: so this relation plays the same role as the "ignition condition" in classical approaches to turbidity currents, and consequently, its fundamental time-scale t^* plays the role of an "ignition time", which explains its name.

8. The steady density-turbidity currents

One other case deserves attention. If a density current crosses a submarine canyon oriented offshore, namely orthogonal to the slope, then in Eq. (7), a sharp increase of $(\partial b/\partial \psi) \sim (\partial b/\partial y)$ pushes the dense current towards the larger depths. However, the same gradient of the sea bottom naturally increases the water velocity U and so, because of the Coriolis force, the dense water moves upward if $\epsilon = 0$ and no water–bottom interaction is to be considered. However, if $\epsilon \neq 0$, then we have that h increases and, consequently, also a small ϵ can allow the formation of a quasi-steady downflow of the dense water current. This elementary mechanism could very well give rise to a steady downflow that pushes the dense water outside the original channel into the open sea, if the balance of the bottom sediments allows a continuous inflow and outflow of bottom particulate. As far as we know, this effect has not been discussed before.

Let us add that also in this steady case an ignition phenomenon has to be considered as the real source of current–bottom particulate interaction. So to clarify its practical role, let us underline how for density currents flowing steadily, if $\nu \sim 10^{-6}$ m^2 s^{-1} as in laboratory simulations, the ignition time t^* necessary for a perturbation to destabilize the current is of the order of 10^7 s. In a more realistic case, one can assume $\nu \sim 10^{-2}$ m^2 s^{-1} as for fully developed turbidity currents; one thus obtains the value $t^* \sim 10^3$ s, which constitutes a much easier triggering effect since oceanic forcings lasting 10^3 s are fairly frequent. These considerations suggest that, in practice, the choice of a realistic value of the friction ν is critical. It is consequently of interest that t^* can realistically be estimated by comparing the two most popular expressions of bottom stress, namely $\tau = \rho C_d U^2$ and $\tau = \rho \nu (\partial U/\partial)$: this gives

$$\tau/\rho \sim \nu \frac{U}{h} \sim C_d U^2 \tag{21}$$

where a realistic $C_d = 3.5 \times 10^{-3}$ (MKS units) can be assumed, and consequently,

$$\nu \sim C_d h U \text{ and so } t^* \equiv \frac{h^2}{\pi^2 \nu} \rightarrow \frac{h}{\pi^2 C_d U} \tag{22}$$

which is a fairly easily applicable relation. Note how this kind of considerations receives support from the linearity of the kinetic energy versus light transmittance shown in Fig. 3, for this period of strong light transmittance variability.

Let us apply these considerations to hydrologic sections along the Antarctic coast. It is immediately apparent that a very dense water is present over the shelf. Its geostrophic velocity can be estimated as 7 cm s^{-1} and the bottom layer is $\sim$ 100 m thick. Consequently, we obtain an "ignition time" $t^* \sim 4 \times 10^4$ s. However, for velocities of $\sim$ 22 cm s^{-1}, one obtains $t^* \sim 10^4$ s and so it is possible that a velocity peak will give rise to a significant mixing of bottom particulate and bottom water, i.e. the starting of a turbidity current.

9. Estimates of entrainment and other quantities

Using these theoretical considerations on bottom current stability, we now have a tool to analyze the main effect evident in our data—the disappearance of DISW in transects D and E (Figs. 2 and 5). In Table 1, we have synthetized the most important data relative to the five transects of the CLIMA cruise.

We first consider the cross-strait balance: from the isopycnals $g' \equiv g(\rho_{DISW} - \rho_{LSSW})/\rho_{DISW}$ and σ_θ on the sea bottom are easily determined (Table 1). It is noteworthy that σ_θ on the sea bottom is constantly decreasing, from south toward north. This clearly shows how DISW is gradually entrained by LSSW as it travels northward. Also of interest is the fact that over the Ross sea shelf the current deflection angle β is very small. Consequently, in the following, we will put $\beta \sim 0$ without fear of serious errors.

Table 1
Summary of the hydrologic values relative to the A–E transects, and $\mathscr{E}^*$ entrainment values

Transect	A	B	C	D	E
$g' \equiv g\Delta\rho/\rho$	9×10^{-4}	9×10^{-4}	9×10^{-4}	5×10^{-4}	10^{-4}
σ_{bottom}	28.00	27.99	27.98	27.91	27.84
h_{DISW}	100	100	100	200	100
h_{LSSW}	150	150	150	150	250
$\Delta\xi$	24×10^{3}	24×10^{3}	24×10^{3}	24×10^{3}	24×10^{3}
W_{DISW}	50×10^{3}	40×10^{3}	30×10^{3}	10×10^{3}	10×10^{3}
$\mathscr{A}_{\text{DISW}}$	5×10^{6}	4×10^{6}	3×10^{6}	2×10^{6}	1×10^{6}
$\mathscr{A}_{\text{LSSW}}$	7×10^{6}	6×10^{6}	6×10^{6}	5×10^{6}	7×10^{6}
U_{measured}	7×10^{-2}				
$U_{\text{estimated}}$		8×10^{-2}	9×10^{-2}	9×10^{-2}	7×10^{-2}
$U-V$	5×10^{-3}	3×10^{-2}	3×10^{-2}	8×10^{-2}	6×10^{-2}
V	8×10^{-2}	11×10^{-2}	12×10^{-2}	17×10^{-2}	13×10^{-2}
ϕ_{DISW}	0.4	0.3	0.3	0.2	0.07
ϕ_{LSSW}	0.6	0.7	0.7	0.8	0.9
$\phi_{\text{DISW}}+\phi_{\text{LSSW}}$	1.0	1.0	1.0	1.0	1.0
$\mathscr{E}^*_\sigma=\mathscr{E}^*$		10^{-3}	2×10^{-3}	3×10^{-3}	6×10^{-2}
$\mathscr{E}^*_\theta$		10^{-3}	10^{-3}	8×10^{-4}	4×10^{-3}
$\mathscr{E}^*_S$		2×10^{-3}	2×10^{-3}	10^{-3}	3×10^{-2}

The hydrologic quantities g', σ_{bottom}, h, $\Delta\xi$ (distance between transects), $\mathscr{A}$, U, V and the fluxes ϕ are computed from the graphs in Figs. 5–8 (MKS system, but fluxes in Sv). The DISW quantities are often observed but, in the absence of field measurements, the theory of density currents is applied. In this way, the transect E quantities are extrapolated assuming $h_{\text{DISW}} \sim 100\,\text{m}$, $U \sim 7\times10^{-2}\,\text{m s}^{-1}$ as from the southern transects. So the $\mathscr{E}^*_\sigma$, $\mathscr{E}^*_\theta$ and $\mathscr{E}^*_S$ estimates of entrainment for transect E are questionable, even if the local disappearance of DISW is quite evident. Note also that we estimate U from the position $\phi_{\text{DISW}}+\phi_{\text{LSSW}}=const.$

Now comparing the continuity Eq. (7) with our data, a more complex situation emerges. First, we estimate $\mathscr{A}_{\text{DISW}}$ and $\mathscr{A}_{\text{LSSW}}$, the cross-section areas for these deep currents. Then we use the $\tilde{H}$ current meter data and compute the corresponding flux, $\phi_{\text{DISW}} \sim 0.4$ Sv, in agreement with previous estimates. The same reasoning shows that the flux of LSSW is $\phi_{\text{LSSW}} \sim 0.7$ Sv. Assuming $\phi_{\text{DISW}}+\phi_{\text{LSSW}}=const$, using the thermal wind equation, we obtain U.

We are now able to investigate the average entrainment $\mathscr{E}$, which for such small velocities is often a vanishing quantity. It must however be pointed out that current meter data show large velocity variations, such that an intermittent $\mathscr{E}$ can easily attain large values. This gives some support to the possibility of large intermittent entrainments, even if the small average velocity corresponds to $\mathscr{E} \sim 0$. To check this possibility, we computed $\mathscr{E}^*$ empirically using volume and mass conservations, as fully discussed in Baringer and Price (1997). This essentially involves considering both Eqs. (1) and (2), which give

$$\mathscr{A}U\frac{\partial\rho}{\partial\xi} = \mathscr{E}(\rho_0-\rho) \simeq \mathscr{E}^* W\,|U-V|\,(\rho_0-\rho) \quad (23)$$

namely a realistic way to estimate $\mathscr{E}^*$ once ρ, U, W, V, $\mathscr{A}$ are known with reasonable accuracy. The computed $\mathscr{E}^*$ are in the Table 1; a reasonable synthesis is that over the Ross Sea shelf $\mathscr{E}^* \sim 10^{-3}$—not a surprising result. It should also be noted how $\mathscr{E}^*$ decreases towards the north, but a jump is evident only for the transect E.

These considerations can be repeated for θ, S or other tracers as well: for θ and S we obtain $\mathscr{E}^*_\theta$ and $\mathscr{E}s^*$ comparable with values of $\mathscr{E}^*$. These estimates do not hold entirely for the northernmost transect E where the DISW is no longer present. However, if we estrapolate the properties of DISW from the other southern transects, in order to obtain σ_θ, θ and S as observed in reality, we need a large value for entrainment, indeed as large as $\mathscr{E}^*=3\times10^{-2}$, in reality corresponding to the disappearance of DISW on the E transect. It is noteworthy how the small value of the "ignition time" t^* supports the likelihood of a bottom particulate–current interaction, as one obtains from an inspection of the light transmission data (Fig. 6). Moreover, the presence of a significant amount of particulate in the near bottom layers of the DISW determines a sort of preconditioning that increases the likelihood of turbidity effects that could play an important role in the disappearance of the DISW close to shelf break. On the other hand, in the case of scarce bottom particulate present in this area, all this gives support to the more physically interesting possibility that a quasi-steady ignition process takes place.

This effect deserves a further comment. Indeed, we have clear how classical, transient turbidity currents can reach their catastrophic ignition point only in presence of a rich quantity of bottom particulate. So both the ignition and the abundance of bottom particulate are necessary conditions. For rather steady density currents, the situation is more complex. Indeed, a rigorously steady density current of velocity v_0 has certainly eroded in the past all the sediments of dimension such that can be eroded by the steady current. So to have any kind of turbidity-density

current, a further condition is necessary, namely a velocity jump that allows the density current to erode some further, slightly denser part of the bottom particulate. This can happen in our case, as shown in Figs. 3 and 4. However, it has to be clear how such density-turbidity effects, although rather difficult to happen, have remarkable effects in deflecting the bottom particulate from unexpected regions into the deepest layers, and also in deflecting the density current from its usual pathway, with remarkable effects also on the bottom particulate evolution.

10. Conclusion

In this study, the northward flow of DISW over the shelf of the Ross Sea is discussed. The flux of this dense cold water is estimated as 0.4 Sv but, once DISW reaches the northern shelf break, this water rather suddenly disappears. This has a deep effect on both the bottom sediments evolution and on this current in such a complex way that all this finally appears as a unique interacting system.

We examined the equation of motion of a density current and focused our attention on the cross-stream momentum equation, which interestingly is decoupled from the other equations and gives the deflection angle β for such dense flows. Indeed, we have some partial, but important, experimental evidence giving support to this last possibility, as the strong correlation between velocity jumps and light attenuation (Fig. 3) and between bottom temperature, salinity and bottom particulate in the lowest layer (Fig. 6). This clearly shows how this angle can be affected by such different physical effects due to bottom topography irregularities, to a vigorous upper layer currents and interactions with the bottom particulate. We unfortunately do not have all the necessary information from existing data but this DISW disappears so quickly that the first two effects do not seem to be the most probable candidates for such downflows. The third possibility, related to the interaction of bottom particulate, is the least investigated of these possibilities but the estimated time scale of this phenomenon, i.e. the "ignition time", is rather small, $\sim 10^4$s, and consequently, turbidity effects probably play an important role, either giving a quick turbidity current or a quasi-steady density-turbidity current. It has to be stressed again how this last idea receives strong support from field observations of light transmission data, showing how over the Ross Sea shelf the density current carries a considerable quantity of bottom particulate, of geological or biological origin. These possibilities can ultimately be clarified only by investigating further data, in particular regarding the size (i.e. surface/value) and the density of this particulate, mainly referring to sediment evolution for this particularly interesting basin. One has to add how similar considerations give a novel insight on both the dense water dynamics as well as on the bottom sediments evolution.

List of symbols

b	bottom depth
x	along-channel horizontal coordinate
y	cross-channel horizontal coordinate
z	vertical coordinate
h_i	the ith interface depth
$\gamma_i = \partial h_i/\partial y$	the ith interface slope
ρ_i	the density of the ith layer
p_i	pressure in the ith layer
ρ	dense water density
V_i	geostrophic along flow velocity of ith layer
f	Coriolis parameter
ζ	streamwise coordinate
ψ	cross-stream coordinate
W	dense water current width
U	velocity as averaged over a cross-section of the dense water current
h	interface of the dense water current
β	bottom current deflection angle
$\mathscr{A} = \int h \mathrm{d}\psi$	dense current cross-sectional area
$\mathscr{E}$	total entrainment of the dense water current
$\mathscr{E}^*$	parameter of entrainment
V	along-channel velocity of the second layer from the sea bottom
$\rho_0(z)$	density of the ambient fluid
$g' = g(\Delta\rho/\rho)$	reduced gravity
$\mathscr{D}$	total bottom drag
(F, F^*)	external forcing acting on the density current
v_s	sediment fall velocity in the lower layer
Δ	hydrologic initial density difference between the last two bottom layers
τ	bottom stress
v	water friction coefficient
B_2, v_0 z_0, q_0	constants
R_i	Richardson number

h_0 steady component of h
Γ_0 steady component of g'
h' time-dependent part of h
Γ' time-dependent part of g'
$t^* = h_0^2/\pi^2 \nu$ turbidity "current ignition time"
ε dimensionless coefficient of nonlinear effects in the evolution equation for h
$\mathscr{V} = \sqrt{\Gamma_0 h_0}$ phase velocity for h'
$h^* = \nu \mathscr{V}/g\epsilon h_0$ critical value for explosive behavior of h'
C_d quadratic friction coefficient
Θ slope of the sea bottom in theoretical computations
ϕ_k flux of the marine water of kth type
$\mathscr{E}_\mu^*$ entrainment coefficient of the tracer μ

Acknowledgements

It is a pleasure to thank Prof. Spezie and Dr. Bouché for their interest and encouragement, and Dr. Azzolini for suggesting this problem. We warmly thank Dr. R. Meloni for providing the current meter data and Dr. S. Tucci for providing the light transmission profiles. We also thank the Italian CLIMA Project for economic support and R. De Gregorio, L. Santonastaso and R. Soldatelli for their substantial help. We also thank F. Stazi for making the drawings in a particularly short time. This study was performed as part of the Italian *National Program for Research Antarctica* (NPRA) and was financially supported by ENEA through a joint research program.

Appendix A

Let us thus consider some layers of water of density ρ_i moving in the along-channel direction. The slopes $\partial h_i/\partial y = \gamma_i \simeq const$ among the various layers give the hydrostatic pressure field

$$\begin{aligned} p_1 &= p_0 + g\rho_1(-z + \gamma_1 y) && \text{in the upper layer} \\ p_2 &= p_0' + g\rho_2(-z + \gamma_2 y) + g\rho_1(\gamma_1 - \gamma_2)y && \text{in the 2nd layer} \\ p_3 &= p_0'' + g\rho_3(-z + \gamma_3 y) + g\rho_2(\gamma_2 - \gamma_3)y + \rho_1 g(\gamma_1 - \gamma_2)y && \text{in the 3rd layer} \\ &\ldots \end{aligned} \tag{A1}$$

Introducing geostrophic along-channel velocities V_i for the ith layer the geostrophic balances give

$$fV_1 \cong g\gamma_1 \quad f(V_2 - V_1) \cong g\gamma_2 \frac{\rho_2 - \rho_1}{\rho_1} \quad f(V_3 - V_2) \cong g\gamma_3 \frac{\rho_3 - \rho_2}{\rho_2} \ldots \tag{A2}$$

where f is the Coriolis parameter. These velocities allow us to simplify Eq. (A1) to

$$\begin{aligned} p_1 &= p_0 - g\rho_1 z + \rho_1 f V_1 y \\ p_2 &= p_0' - g\rho_2 z + \rho_1 f V_2 y \\ p_3 &= p_0'' - g\rho_3 z + \rho_1 f V_3 y \\ &\ldots \end{aligned} \tag{A3}$$

Note that if the marine bottom is not particularly regular, a geographical deflection and a centrifugal force have to be taken into consideration: Eq. (A2) hold as long as centrifugal effects are smaller than, say, the Coriolis force.

References

Astraldi, M., Gasparini, G., Gervasio, L., Salusti, E., 2001. Dense water dynamics in the Strait of Sicily. J. Phys. Oceanogr. 12, 3457–3475.

Baringer, M., Price, J., 1997. Momentum and energy balance of the Mediterranean outflow. J. Phys. Oceanogr. 27, 1678–1692.

Bignami, F., Mattietti, G., Schiarini, S., 1990. Observation on a bottom vein of dense water in the Southern Adriatic and Ionian Seas. J. Geophys. Res. 95 (C5), 7249–7259.

Budillon, G., Spezie, G., 2000. Thermohaline structure and variability in the Terra Nova bay polynya (Ross Sea) between 1995–1998. Antarct. Sci. 12 (4), 501–516.

Budillon, G., Tucci, S., Artegiani, A., Spezie, G., 1999. Water masses and suspended matter characteristics of the western Ross Sea. In: Faranda, F.M., Guglielmo, L., Ianora, A. (Eds.), Ross Sea Ecology. Springer-Verlag, Milan, pp. 63–93.

Budillon, G., Fusco, G., Spezie, G., 2000. A study of surface heat fluxes in the Ross Sea (Antarctica). Antarct. Sci. 12 (2), 243–254.

Caserta, A., Mieli, E., Salusti, E., 1990. On a model of bottom erosion by dense water steady veins. Geophys. Astrophys. Fluid Dyn. 5S, 117–135.

Drazin, P., Reid, W., 1981. Hydrodynamic Stability. Cambridge Univ. Press, Cambridge, 525 pp.

Ellison, T., Turner, J.S., 1959. Turbulent entrainment in stratified flows. J. Fluid Mech. 6, 423–448.

Emms, P., 1997. Streamtube models of gravity currents in the ocean. Deep-Sea Res. 44, 1575–1610.

Harvey, D., 1996. Polar boundary layer plumes and bottom water formation: a missing element in ocean general circulation models, J. Geophys. Res. 110 (C9), 20, 799-20, 808.

Hofman, E.E., Klink, J.M., 1998. Hydrography and circulation of the Antarctic continental shelf: 150E to the Greenwich Meridian. In: Robinson, A.R., Brink, K.H. (Eds.), The Sea, vol. 11, pp. 997–1042.

Jacobs, S.S., 1989. Marine controls on modern sedimentation on the Antarctic continental shelf. Mar. Geol. 85, 121–153.

Jacobs, S.S., 1991. On the nature and significance of the Antarctic slope front. Mar. Chem. 35, 9–24.

Jacobs, S.S., Amos, A.F., Bruchhausen, P.M., 1970. Ross Sea oceanography and Antarctic bottom water formation. Deep-Sea Res. 17, 935–962.

Jacobs, S.A., Fairbanks, R.C., Horibe, Y., 1985. Origin and evolution of water masses near the Antarctic continental margin: evidence from H2180/H2160 ratios in seawater. In: Jacobs, S.S. (Ed.), Oceanology of the Antarctic Continental Shelf, vol. 3, pp. 59–85.

Jaeger, J., Nittrouer, C., De Nastor, D., Klechner, C., Dumbar, R., 1996. Lateral transport of settling particles in the Ross Sea. J. Geophys. Res. 101 (C8), 18.479–18.488.

Killworth, P., 1983. Deep convection in the world Oceans. Rev. Geophys. Space Phys. 21, 1–26.

Kurtz, D.D., Bromwich, D.H., 1983. Satellite observed behaviour of the Terra Nova Bay polynya. J. Geophys. Res. 88, 9717–9722.

Kurtz, D.D., Bromwich, D.H., 1985. A recurring atmospherically-forced polynya in Terra Nova Bay. In: Jacobs, S.S. (Ed.), Oceanology of the Antarctic Continental Shelf, vol. 43, pp. 177–201.

Locarnini, R.A., 1994. Water masses and circulation in the Ross Gyre and environs. Dissertation for the PhD, A&M University, 87 pp.

Parker, G., Fukushima, Y., Pantin, H.M., 1986. Self accelerating turbidity currents. J. Fluid Mech. 171, 145–181.

Pedlosky, J., 1979. Geophysical Fluid Dynamics. Springer-Verlag, New York, 624 pp.

Picco, P., Amici, L., Meloni, R., Langone, L., Ravaioli, M., 1999. Temporal variability of currents in the Ross Sea (Antarctica). In: Spezie, G., Manzella, G. (Eds.), Oceanography of the Ross Sea Antarctica. Springer-Verlag, Milan, pp. 103–117.

Plapp, J.E., Mitchell, J.P., 1960. A hydrodynamic theory of turbidity currents. J. Geophys. Res. 65, 983–992.

Salusti, E., 1996. A new model for marine density turbidity currents with criteria for ignition. Geophys. Astrophys. Fluid Dyn. 83, 233–260.

Smith, P.C., 1975. A streamtube model for bottom boundary currents in the Ocean. Deep-Sea Res. 22, 853–873.

Stacey, A., Bowen, J., 1988a. The vertical structure of density and turbidity currents: theory and observation. J. Geophys. Res. 93, 3528–3542.

Stacey, B., Bowen, J., 1988b. The vertical structure of turbidity currents and a necessary condition for self-maintenance. J. Geophys. Res. 93, 3543–3553.

Sugimoto, T., Whitehead, J., 1983. Laboratory models of bay-type continental shelves in the winter. J. Phys. Oceanogr. 13 (10), 1819–1828.

Trumbore, S.E., Jacobs, S.S., Smethie Jr., W.M., 1991. Chlorofluorocarbon evidence for rapid ventilation of the Ross Sea. Deep-Sea Res. 38 (7), 845–870.

Tucci, S., Ferrari, M., Capello, M., 1999. Actual sedimentation on the Antarctic continental shelf (southern part of the Ross Sea). In: Spezie, G., Manzella, G. (Eds.), Oceanography of the Ross Sea (Antarctica), Springer-Verlag, Milan, pp. 197–207.

Turner, J.S., 1986. Turbulent entrainment: the development of the entrainment assumption, and its application to geophysical flows. J. Fluid Mech. 173, 431–471.

UNESCO, 1983. The acquisition, calibration and analysis of CTD data. A report of SCOR WG 51. Technical Papers in Marine Science, pp. 54–59.

UNESCO, 1988. Algorithms for computation of fundamental properties of seawater. Technical Papers in Marine Science, pp. 44–53.

Whitham, G.B., 1974. Linear and Nonlinear Waves. Wiley, New York.